MRI Investigations of Fractures and Multiphase Flow in Fractured Media

Songhua Chen, Xiaoli Yao, Jinli Qiao, and A. Ted Watson
Dept. of Chemical Engineering, Texas A&M University, College Station, TX 77843

The new application of nuclear magnetic resonance imaging (MRI) techniques for characterizing fractures and flow in fractured media is investigated. Specifically, a relaxation-weighted imaging technique is used for selectively highlighting either fracture or porous matrix regions. Many advantages over conventional spin-density MRI techniques for characterizing fractured media are demonstrated. Its use to speed image acquisition is also demonstrated. In addition, a multislice profile imaging technique is used to investigate imbibition and drainage displacement experiments in fractured porous media. These images demonstrate that the fractures can have profound effects on the fluid distributions in multiphase flow.

Introduction

Understanding and simulating multiphase flow through porous media have long been key and challenging issues to industry directed to the extraction of fluids from petroleum reservoirs as well as to the characterization and remediation of aquifers. Fractured porous media systems are among the most difficult to model, particularly as they represent systems for which structural and petrophysical properties vary by orders of magnitudes. The lack of suitable experimental methods has been a major limitation to the advancement of dynamic models for multiphase flow through fractured systems.

Experimental characterizations of fluid distributions and multiphase displacements are important issues for model development since these two aspects are essential to major engineering focuses on fractured reservoir systems, such as developing effective fracturing processes or enhancing production from fractured reservoirs (Economides and Nolte, 1988). An experimental technique useful for investigating fractured systems should have several basic capabilities. First of all, adequate spatial resolution and sensitivity are required to characterize the fractures, pore structures in the matrix regions, and fluid-phase distributions. In addition, the ability to observe individual fluid phases is necessary for multiphase processes. In this article, we address the development of nuclear magnetic resonance imaging (MRI) applications that have many pertinent features for monitoring structural and dynamic flow studies of fractured porous media systems.

Previously, MRI techniques have been proven useful for quantitative determination of fluid-phase saturation distributions in static and dynamic experiments (Chen et al., 1993, 1994; Fordham et al., 1994) in relatively homogeneous porous media. There are special challenges for MRI applications to fractured permeable media typical of underground reservoir formations. In particular, accurate fracture characterization will be difficult for fractured systems having insignificant contrasts between fracture and porous matrix, or for which there are variations in porosity resulting from other means, such as bedding planes. In the first part of the article, a new application of relaxation-weighted MRI technique is demonstrated for characterizing fractures and porous matrix. Through selection of the imaging protocol, the signal from *either* the fractures or porous matrix regions can be highlighted, while the other signal is virtually eliminated. A similar approach (Bydder and Young, 1985; Dwyer et al., 1988; Mascalichi et al., 1993) has been reported previously in medical applications for the investigation of lesions and for enhancing contrasts between tumor and fat/muscle; however, its application to fractured systems has not been explored. Considerable advantages of this technique compared to conventional spin-echo imaging (Morris, 1986) for investigating fractured media are demonstrated. A method for rapid imaging acquisition using this technique is presented.

In the second part, MRI investigation of multiphase displacement processes in fractured systems is reported. Drainage and imbibition displacement experiments were conducted in fractured sandstone samples. A multislice nuclear magnetic resonance (NMR) imaging technique was used to obtain unique information regarding the fluid distributions in fractured systems.

Current address of S. Chen: Western Atlas International Inc., 10205 Westheimer, Houston, TX 77042.

Theory

Conventional NMR spin-density images, for which the intensity is proportional to the amount of the observed fluid phase, can in principle be used to characterize fractures in fluid-saturated porous media, provided that there are sufficient contrasts between the amounts of fluid occupying pixels associated with the fractures and porous matrix. The mapping of fracture distributions and estimation of fracture sizes would then require a discrimination method based on assumed properties or other empirical means, similar to those used with x-ray computed tomography (CT)-scanning (Watson and Mudra, 1994; Lu et al., 1994). The conventional spin-echo imaging technique will not be suitable for systems without adequate porosity contrast between pixels in fractures and matrix regions, in which case, fractures will be difficult to discern. Nor will it be suitable for systems in which the spin-density is much greater in the fractures than in the matrix; in those cases the determination of fluid distributions in matix regions may be overshadowed by strong signals in the fracture pixels, resulting in a poor signal-to-noise (S/N) ratio in the matrix regions. In this article we investigate an imaging technique that can overcome such limitations of the conventional spin-echo imaging techniques.

The rationale of our approach described below is based on the feature that the observed NMR relaxation rate in porous media is dominated by relaxation at surfaces (Brownstein and Tarr, 1977). In the fast diffusion approximation, the observed T_1 for individual pores is expressed as (Brownstein and Tarr, 1977, Banavar and Schwartz, 1989)

$$\frac{1}{T_{1i}} = \frac{1}{T_{1b}} + \frac{\lambda}{T_{1s}} \frac{S_p}{V_p}, \tag{1}$$

where S_p and V_p are the pore surface and pore volume, T_{1b} and T_{1s} are the bulk and surface relaxation times, respectively, and λ is the thickness of the surface fluid layer. For most pores of reservoir rock systems, the second term in Eq. 1 is dominant since the surface relaxation is fast. Based on Eq. 1, we can expect the relaxation times for fluid protons in fractures and in the porous matrix to be quite different, since the former has much smaller surface-to-volume ratios than the latter, and thus the relaxation contrast can be used for distinguishing fractures from matrix.

The pulse sequence we used is the inversion-recovery spin-echo (IRSE) imaging sequence (Bydder and Young, 1985) (Figure 1), which includes two functional parts. The first part (IR) can be used to suppress the signal from the selected region. Suppose that fluid in one of the regions can be approximately characterized by relaxation time T_1. Then the time evolution of the magnetization is described by

$$M(TI) = M_0[1 - 2\exp(-TI/T_1)], \tag{2}$$

provided that the repetition time between acquisitions is much longer than T_1. Note that the signal from that region would be suppressed if the inversion time TI were selected so that

$$TI_0 = T_1 \ln 2. \tag{3}$$

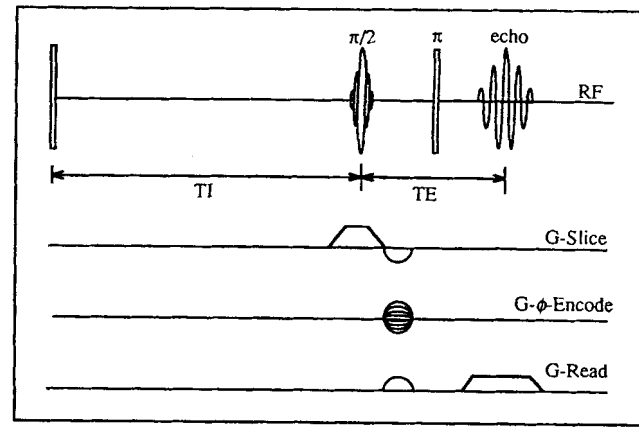

Figure 1. IRSE imaging sequence.

Obviously, TI_0 would be different for signals having different relaxation times T_1.

Consider now the application of a spin-echo (SE) sequence after the inversion recovery. The magnetization decay is described by

$$M(TI + TE) = M_0 \exp(-TE/T_2)\{1 - 2\exp(-TI/T_1) + 2\exp[-(TR - TE/2)/T_1] - \exp(-TR/T_1)\}, \tag{4}$$

where TR is the repetition time. For fluids in porous media, T_2 is short so that a small TE has to be chosen to observe the signal. Therefore, $TE \ll TR$ is generally valid, in which case the preceding expression can be simplified to

$$M(TI + TE) = M_0 \exp(-TE/T_2)[1 - 2\exp(-TI/T_1) + \exp(-TR/T_1)]. \tag{5}$$

The signal can be eliminated by selecting TI so that

$$TI_0 = T_1 \ln \frac{2}{1 + \exp(-TR/T_1)}. \tag{6}$$

The preceding expression is based on the assumption of the validity of a single T_1 for the entire region under investigation. The spins in the fractures may be suitably treated as relaxing at a single rate. However, the relaxation in the pore matrix usually is not well represented with a single exponential. If one uses a stretched exponential function to describe the decay in the rock matrix, the magnetization corresponding to the fluid in the matrix is minimized at

$$TI_m = TI_\alpha = T_{1\alpha}(\ln 2)^{1/\alpha}, \tag{7}$$

where the repetition time $TR \gg T_{1\alpha}$ is assumed. This assumption is reasonable considering that $T_{1\alpha}$ in porous matrix is much shorter than that in fractures, so that the condition is easy to satisfy. Note that the existence of signal nulling TI is independent of the relaxation decay model, since it is a feature of the inversion-recovery sequence. A relaxation model is not necessary for determining the TI corresponding to a

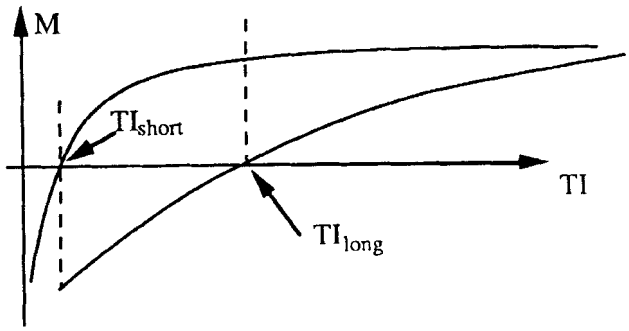

Figure 2. Fast and slow relaxation decay curves.

null signal. The *TI* value can be selected from experiments with several trial values using one-dimensional (1-D) acquisitions.

A diagram of the decay curves for fluids with two characteristic relaxation rates is shown in Figure 2. In this illustration, the two decay curves differ greatly in T_1. For such a case, one can suppress either of the signals by selecting the *TI* value. While the intensity of one of the signals is suppressed, the intensity of the other signal is not affected significantly. This selection can be used to highlight the signals from either the porous matrix or fractures in fluid-saturated porous systems. To highlight the fractures, one can eliminate signals from the porous matrix by choosing the inversion time that satisfies Eq. 6 using $T_1 = T_{1\text{fracture}}$. On the other hand, to highlight the details of the porous matrix, one can choose the inversion time to satisfy Eq. 7.

Another advantage of the present approach is the capability of achieving faster image acquisitions. From Eq. 6, we see that for a shorter repetition time, the null of the signal should occur at a shorter *TI* compared to $TI_0 = 0.69T_1$ for $TR \rightarrow \infty$. This feature allows one to choose a smaller value of TI_0 with a shorter repetition time *TR* to achieve the reduction of the total imaging time. We discuss later the applications of using the short repetition time to highlight the fluid distributions in the matrix without sacrificing signal intensity.

We note that the capability of highlighting either fractures or porous matrix is a unique advantage provided by the IRSE sequence. Neither CT scanning nor conventional MRI with *TE* weighting has similar capabilities.

Experimental Procedures

The samples used in this study include sandstones (Arkansas-Gold and Berea) and limestones (Indiana and Calico). Those samples were cored 2.54 cm in diameter with lengths ranging from 3.8 cm to 5.7 cm.

The Calico limestone sample contains a natural fracture. For the rest of the samples, artificial fractures were cut parallel to the cylindrical axes of the samples. The width of the fractures was controlled by sandwiching in one or two layers of sieved glass beads. The sizes of the inserted beads range from 0 (no beads added) to 250 μm for different samples. The pore volume in the fracture was controlled by the amount of beads inserted between the pieces of the core samples. Epoxy-sealant was applied on the cylindrical surfaces and on the edges of the fractures. During measurements, the locations of the fractures were searched using 1-D profiles. Then the sample was oriented so that the fractures were parallel to the horizontal direction.

All NMR measurements were performed in a GE 2-Tesla Omega CSI system with a 4.45-cm-i.d. birdcage rf coil under a regulated room temperature. Most of the images were acquired at $TE = 3.1$ ms, the minimum echo time allowed by the system for 2-D images, unless stated otherwise. Repetition times $TR \geq 4T_1$ were used, except as stated otherwise. The frequency encoding gradient strengths used in these experiments were 0.098 T/m, applied in the direction perpendicular to the cylindrical axis of the samples. Image resolution of 256 pixels in each dimension was used with the size of the pixel to be 0.15 mm ($\approx$ 660 Hz). For samples with linewidths narrower than this, the pixel size represents the true resolution. However, certain samples exhibit broader linewidths; in those cases, the true resolution will be reduced. Detailed discussion of the resolution is presented in a subsequent section. The slice thicknesses of the 1-D and 2-D images are 5 mm for static cases, and 4 mm for dynamic experiments, unless stated otherwise.

Water was used as the saturating fluid for the fracture and porous matrix characterization experiments. For the two-phase experiments, deuterium oxide (D_2O) and hexadecane were used as the aqueous and oleic phases, respectively. Thus, the measured NMR signals correspond to the oleic phase.

Results and Discussion

Fracture detection in low-porosity contrast systems

We first show the results of fracture detection in two rock systems, Indiana limestone and Arkansas Gold sandstone core plugs, with very small fracture widths. Artificial fractures were made with the fracture planes perpendicular to the cross sections of the samples. No glass beads were placed within the fractures; the fracture spacings are then due only to the slightly less-than-perfect matching of the sections of the samples after cutting and sealing. The two samples provide a good basis for testing the imaging technique. The NMR linewidths are fairly representative of the respective rock types (320 Hz for Indiana limestone and 1,150 Hz for Arkansas Gold). The Indiana limestone has a broad range of pore sizes. It exhibits two characteristic pore sizes, with relatively longer T_1 values associated with the primary pore systems, and relatively short values with the secondary pores. It is desirable that the imaging technique provides sufficient matrix/fracture contrast for such systems.

Figures 3a and 3b show 1-D profile images for a single cross section of the Indiana limestone sample, while Figures 3c and 3d show the profiles for the Arkansas Gold sandstone sample. These profiles were obtained with the inversion time $TI = 5$ s for Figures 3a and 3c and $TI_{0\text{matrix}} = 400$ ms and 290 ms for Figures 3b and 3d, respectively. Thus, Figures 3a and 3c are equivalent to standard spin-echo images since, with such a long *TI*, spins have recovered from the T_1 effect. From the intensity variations of the profile shown in Figures 3a and 3c, no clear evidence of a fracture is observed. However, with suitable selection of *TI* for eliminating signals from the matrix region, the fractures are readily identified (Figures 3b and 3d). Note that in Figure 3a, there is a decrease in the intensity at the location where the fracture should be observed. Thus the fracture contains less fluid than a corre-

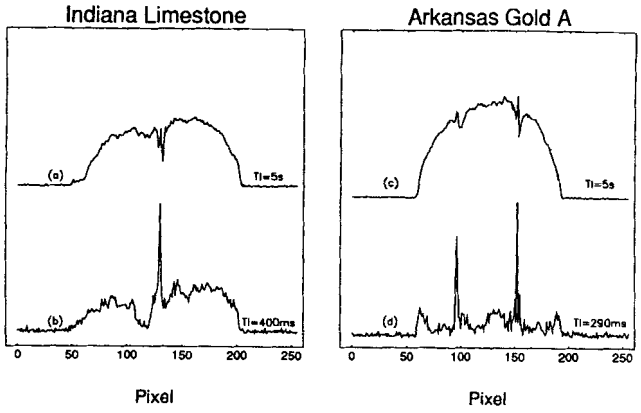

Figure 3. 1-D slice profiles of a single cross section for (a) and (b) an Indiana limestone and (c) and (d) an Arkansas Gold sandstone.

For (a) and (c), $TI = 5$ s; for (b) $TI_{0\text{matrix}} = 400$ ms; for (d) $TI_{0\text{matrix}} = 290$ ms.

sponding volume of the porous matrix, which seems contradictory to what one might expect. This may be due in part to a reduction in the fracture pore space caused by invasion of the epoxy sealant. Evidently, this situation does clearly demonstrate the effectiveness of the *TI*-weighting technique for identifying fractures in porous systems.

Note that the signal in the matrix region was not completely eliminated in Figure 3b (the IRSE image for Indiana limestone). It is likely that the residual signal is largely from the primary pores in the matrix region, since primary pores are larger and correspond to longer relaxation times that are not completely eliminated at the experimentally selected inversion time *TI*. In contrast, signals in the matrix were almost completely eliminated in Figure 3d for Arkansas Gold sandstone, which does not have distinctive primary and secondary pores.

Highlighting fractures or porous matrix regions in laminated systems

In the previous subsection, we discussed the method for identifying fractures for difficult cases that have poor spin density contrasts between pixels in fractures and porous matrix regions. In this subsection, we demonstrate the utility of the technique for investigating laminated systems with fractures. Systems with sedimentary laminations often have different porosities associated with different laminae. For characterizing such systems, one usually faces two problems. When thin fractures occur parallel to the bedding planes, the porosities in the fractures and in some higher-porosity bedding planes could appear at similar intensities, and thus it would be difficult to distinguish one from the other based on porosity (or spin density) contrast. On the other hand, when large fractures are present, pore structural features, such as porosity variations across the bedding plane, can be overshadowed by the strong signal in the fractures. We found that T_1 relaxation times for fluids in the fracture and in bedding planes are usually different, which allows the use of the relaxation-weighted technique for discerning fractures from bedding planes or for highlighting matrix regions.

A Berea sandstone with two artificial fractures that are parallel to the bedding planes was used. We had approximately two layers of beads filled in the fractures. For one fracture, glass beads of size 180–250 μm and 63–90 μm were filled in the fracture to obtain a low porosity. A much smaller amount of 180–250 μm beads was placed inside the second fracture so that a different (higher) porosity was obtained. The sample was so prepared to represent a reservoir situation for which fractures have been partially filled by sand or proppant. Figure 4a and 4b show the 2-D cross section images that correspond to $TI = 4$ s and $TI_{0\text{matrix}} = 220$ ms, respectively. On Figure 4a, one can easily identify one fracture on the left, but the other one is not so readily identified. This demonstrates the difficulty one may have in distinguishing low porosity fractures from bedding planes when using spin-density-contrast images. For those cases, the elimination of the signal from the porous matrix with the *TI*-weighted imaging technique is useful. In Figure 4b, we can unambiguously identify the two fractures. The necessity of using the relaxation weighting technique for discerning fractures from rival-porosity bedding planes is also true for the 1-D profiles (Figures 5a and 5b) for the same slice.

On the other hand, in order to highlight the porous matrix structure, we select $TI = TI_{0\text{fracture}}$ so that the signals from the fractures are eliminated. Then experimental data-acquisition conditions (such as the amplifier gain) that are more suitable for imaging the weak signals in the porous matrix

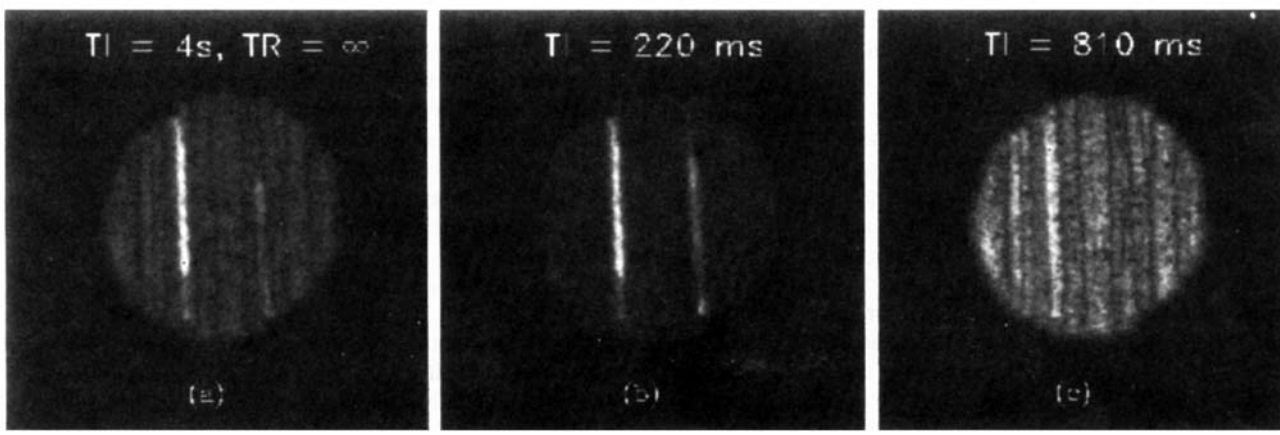

Figure 4. 2-D images of a single cross section for a Berea sandstone.

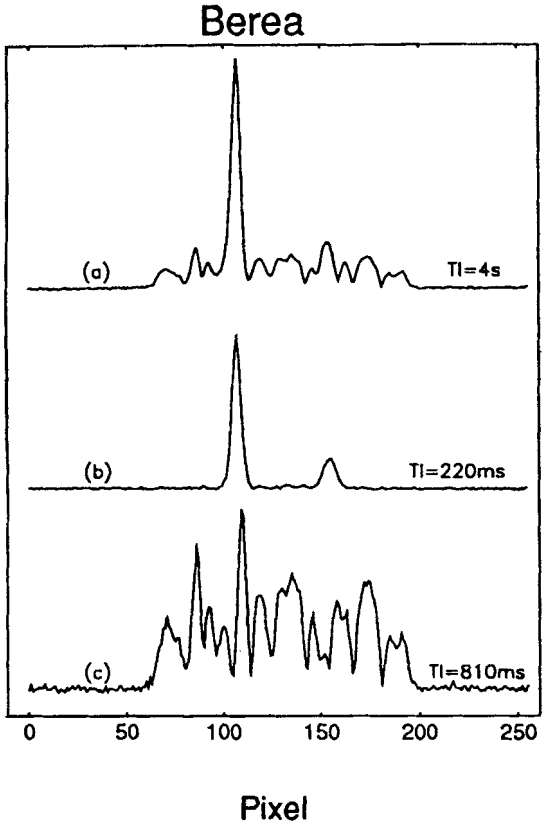

Figure 5. 1-D profiles of the same sample and cross section as shown in Figure 3.

The three profiles correspond to (a) $TI = 4$ s; (b) $TI_{0m} = 220$ ms; and (c) $TI_{0f} = 810$ ms.

can be selected, thereby boosting the S/N ratio in that region. Examples are shown in Figures 4c and 5c. They were acquired with $TI_{0\text{fracture}} = 810$ ms. The images provided much better contrast for the laminations than Figures 4a and 5a. The capability of improving the S/N ratio is particularly important for 2-D image acquisitions, considering the smaller spin density in each 2-D pixel.

Investigation of low-permeability naturally-fractured rock with rapid imaging acquisitions

Highlighting porous matrix structures is also very important for the investigation of fluid distributions in low permeability fractured rocks, since these tend to have very short T_2^* and small amounts of fluid. A naturally fractured Calico limestone was selected for study. The permeability of a companion sample that is not fractured is less than 10^{-3} μm^2. The value of T_2 is 1.3 ms for fluid in the porous matrix. The spin-echo image with $TE = 3.1$ ms reflects a TE weighting for which the signal intensity in the matrix region is substantially reduced, allowing the fracture to be readily identified (see Figures 6a and 7a). However, the signal for the porous matrix is too low to be meaningful, even from the 1-D profile (Figure 7a). Only after the strong signal from the fracture is suppressed by using the $TI_{0\text{fracture}}$-weighted approach (Figures 6b–6d and 7b–7d) can the details of the porous matrix be revealed. The great improvement of the S/N ratio for the

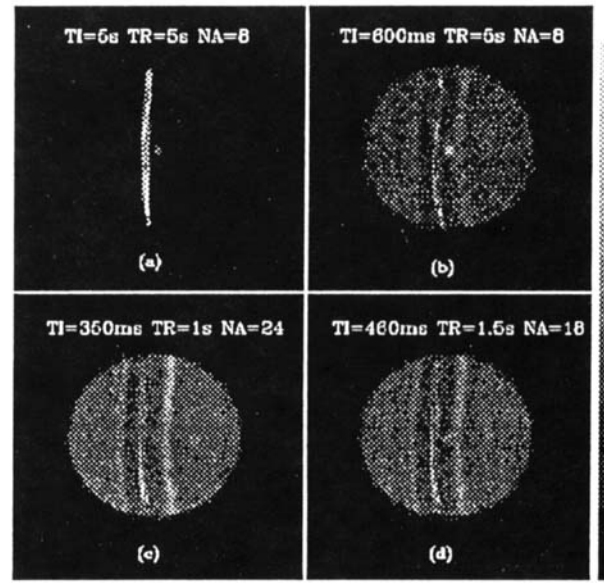

Figure 6. 2-D images of Calico limestone with a natural fracture.

Table 1. Values for the Images in Figure 6

Image	TR	TI_0^{cal}	TI_0^{exp}
Figure 6b	5 s	597 ms	600 ms
Figure 6c	1.5 s	458 ms	460 ms
Figure 6d	1 s	362 ms	350 ms

matrix region would be important if quantification of fluid distributions in the matrix is required.

An advantage of the TI-weighted IRSE technique for imaging porous matrix regions is that different TR and TI_0 pairs can be used to speed image acquisition. At each given TR, the values of $TI_{0\text{fracture}}$ can be obtained either experimentally or calculated theoretically, provided that the decay model is determined. Unlike fluids in porous matrix regions, relaxation decay of fluid in fractures can be approximately represented by a single exponential model, and thus Eq. 5 can be used. For the Calico limestone sample, the value of $T_{1\text{fracture}} = 860$ ms was obtained by using a single exponential. Using that value, R and $TI_{0\text{fracture}}^{cal}$. The values for the three images shown in Figures 6b–6d were determined and are listed in Table 1, along with the experimentally determined $TI_{0\text{fracture}}^{exp}$. The values of $TI_{0\text{fracture}}^{exp}$ were chosen so that signals in the fracture were minimized in every case. The parameter was obtained by comparing several 1-D profiles obtained with TI values in the neighborhood of $TI_{0\text{fracture}}^{cal}$, each differing by a step of $\Delta TI = 10$ ms. The fact that the $TI_{0\text{fracture}}^{exp}$ and $TI_{0\text{fracture}}^{cal}$ values are very close to each other indicates that the single exponential model is indeed appropriate for fluid in fractures.

Comparing Figures 6b–6d, it is easy to see that the image quality is best for Figure 6c and poorest for Figure 6b. Yet, because of the shorter repetition time for acquiring the image of Figure 6c, it allows more signal averages and 40% less total imaging time compared to Figure 6b. For Figure 6d, both the S/N ratio and total imaging time are between the other two cases.

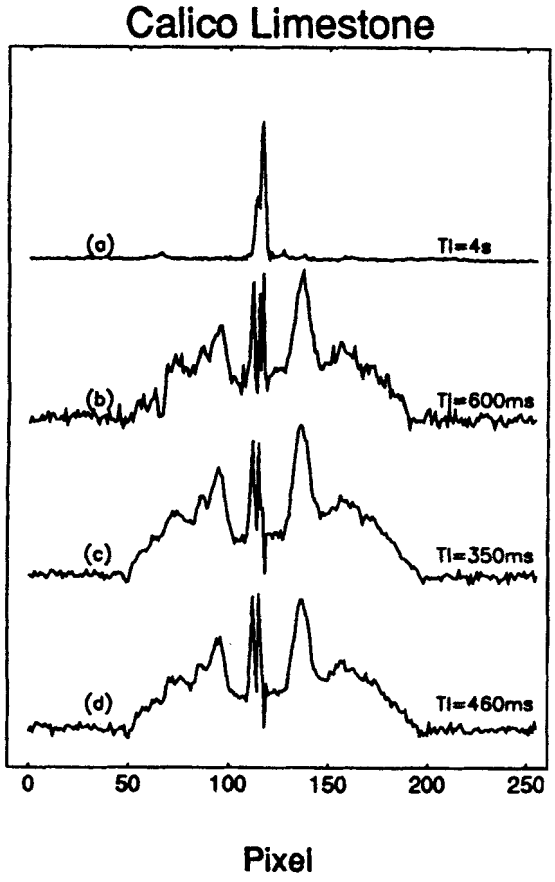

Figure 7. Comparison of 1-D profiles obtained with different *TI* and *TR*.

Discussion of the resolution

There are several factors that can affect the estimate of fracture size. Some factors are related to properties of the fractured system itself, while others are related to the sample orientation during the measurements. The first category includes inhomogeneous line broadening and the variation of fracture width with position. The second category is related to the alignment of fractures with the frequency-encoding gradient for 1-D experiments.

The line-broadening problem is an intrinsic effect that affects both 1-D and 2-D images. Increasing the read gradient strength may compensate the problem to a certain extent. In our experiments, a read gradient (frequency-encoding gradient) of 0.098 T/m was used, which corresponds to a resolution of 150 μm/pixel (660 Hz/pixel). It is then expected that there will be signal overlap among adjacent pixels in samples with broad lines, particularly for Berea sandstones that have linewidths typically ranging from 2,300 to 3,500 Hz. The fracture width determined from Figure 4b is 900 μm, which is significantly broader than that corresponding to the width of the two layers of inserted beads (500 μm). The magnitude of the difference is consistent with the effect of broad linewidths. In contrast, the linewidths are 320 Hz for Indiana limestone and 1,070–1,260 Hz for Arkansas Gold; there will be no line-broadening effects on the fracture width determination for the former, and only a minor effect for the latter.

The roughness of the fracture surfaces in natural fractures can also smear the otherwise sharp distinction between fracture and matrix, thus contributing to a small uncertainty in fracture-width determination. This effect will exist independently of the measurement technique that is used.

The estimation of fracture widths from the 1-D profile images can also be affected by the orthogonality of the gradient relative to the fractures, the straightness of the fractures, and the image slice thickness if the fracture plane or planes are not perpendicular to the cross section of the slice. The straightness of fractures is also a concern when using 2-D imaging with a thick slice. The problem will not be severe for many natural fractures that occur in roughly straight layers, as well as in experiments designed to study flow with MRI, which may typically deal with artificial straight fractures. The rapidity and S/N ratio gained from the 1-D image acquisitions often justifies the 1-D technique, even with a little sacrifice of fracture width accuracy.

The fracture width of 300 μm appearing in the image (Figure 3b) for Indiana limestone is broader than expected for the sample, since no beads were inserted in the fracture and the NMR linewidth is sufficiently narrow that the line-broadening effect does not apply to this case. It is found that the observed broader fracture width may be caused by epoxy invasion into the fracture space during the fracture preparation and sealing. This epoxy invasion, which has been visually observed by breaking up the sample after the NMR measurements, has caused the fracture width to expand slightly after the epoxy had cured. Thus the 300-μm fracture width observed is quite reasonable for this sample. For the Arkansas Gold A sample, special care was taken during the sample preparation to ensure that narrowly spaced fractures were obtained. Indeed, a small fracture width ($\approx$ 200 μm) was observed in Figure 3d for the Arkansas Gold sample.

Two-phase displacement in fractured rocks

Two displacement experiments are described in this subsection. For both experiments, Arkansas Gold sandstones with artificial fractures were used. The samples were prepared so that the ends of the fractures were sealed with epoxy-sealant, representing embedded fractures. Average properties measured on a companion sample were $k = 14.6$ nm^2 and $\phi = 14.4\%$. In the first experiment, D_2O was injected into a sample that was saturated with oil. In the second experiment, oil was injected into a D_2O-saturated sample.

Water Injection. Deuterium oxide (D_2O) was injected consecutively at three different rates: 2 cm^3/h, 8 cm^3/h, and 20 cm^3/h. Each flow rate was kept for a sufficiently long time to achieve an apparent equilibrium before stepping to the next injection rate. Multislice 1-D profile images (Chen et al., 1993), representing oil saturations in the different cross sections perpendicular to the flow direction, were used to monitor the saturation variations.

Ten slices were observed during the experiment. To illustrate the difference in displacement features at different locations along the flow direction, we plot in Figures 8a–8c the oil-intensity profiles corresponding to three slices located: (a) 2 mm from the inlet, (b) 3 mm off the center (bias to the inlet); and (c) 4 mm from the outlet of the core sample, re-

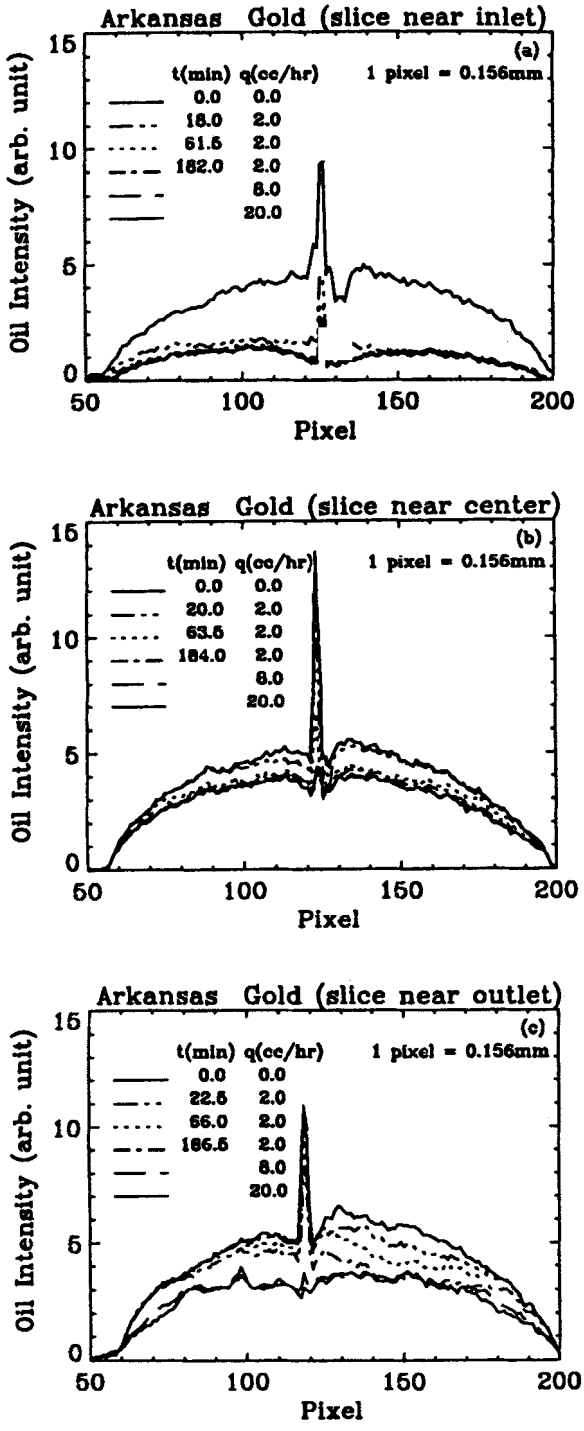

Figure 8. Time-dependent oil intensity profiles of an Arkansas Gold sandstone sample obtained at different times during an experiment with D_2O displacing hexadecane.

The three plots correspond to three locations along the core sample.

spectively. The slice thicknesses are $\Delta z = 4$ mm and the pixel resolution $\Delta l_p = 0.15$ mm. Each profile represents the oil intensity at different times during the displacement experiment. On each figure, the first profile, which has the highest oil intensity, corresponds to $S_o = 1$; the next three profiles were all taken during the displacement with the flow rate $q = 2$ cm^3/h, but at different times; the final two profiles were obtained at the ends of the displacement stages with flow rates $q = 8$ cm^3/h and $q = 20$ cm^3/h, respectively. Since a cylindrical sample was used in the study, the intensities of the profiles for the circular cross sections correspond to the hypotenuse-weighted intensities, that is, the sample volume of each pixel is proportional to the length of the hypotenuse perpendicular to the frequency encoding gradient. Since the hypotenuse corresponding to each pixel is different for a circular cross section, a rounded-enveloped profile would be expected for the sample region if a homogeneous sample is used (see Chen et al., 1993 for a detailed discussion of this topic).

The flow behavior is quite different from that exhibited by the regular saturation changes observed in relatively uniform media (Chen et al., 1993, 1994). In each of the three regions, the oil intensity decreases from the initial saturation state as oil is displaced. As expected, the decrease occurs first in the slice near the inlet, and then at successively later times at positions farther from the inlet (see Figure 8). Note, however, that the change in the saturation in the slice near the center of the core region is considerably less than the slice near either the inlet or the outlet. Water enters the sample through the porous matrix (because the fracture is sealed), and relatively quickly sweeps much of the oil from the entrance region. In the central region, however, relatively little change in the signal intensity occurs in the porous matrix region, indicating that water is preferentially flowing through the fracture. At the outlet, where the fracture is sealed, the water again sweeps the oil from the porous matrix, although not to the degree that occurred in the initial section. Note that the oil is displaced from the fracture region, which is located near the center of the figures.

Oil Injection. The injection of oil into a water-filled sample can simulate the situation of nonaqueous phase contaminants entering aquifers. In our experiment, the sample is initially saturated with D_2O, and hexadecane is injected using the flow rate $q = 4$ cm^3/h. Figure 9 shows the oil intensity during the displacement process. The ten plots correspond to ten different cross-sections along the flow direction. From inlet to outlet, these plots correspond to cross-section slices 5 mm apart, except between Figures 9i and 9j; there the spacing is 7 mm in order to position the slice closer to the end of the sample. On each plot, the lowest intensity profile, which is at the baseline, corresponds to the initial state. The gradient was aligned according to the lefthand side fracture. The righthand side one appears artificially broadened since the two fractures were not exactly parallel to each other.

As in the first experiment, the greatest changes in the saturation distributions occur near the inlet (Figure 9a) and outlet (Figure 9j) of the sample. This is due to the fact that the ends of the fractures are closed. Flow in the fracture seems to be particularly dominant in this experiment. The saturation in the fractures seems to change very quickly, and then remain constant, whereas in the previous experiment the saturation seems to change over a greater range of time. Also, the saturation distributions in the porous matrix region appear to change more slowly than in the previous experiment. These observations would seem to be consistent with a water wet porous matrix material.

Although the saturation distributions in the porous matrix

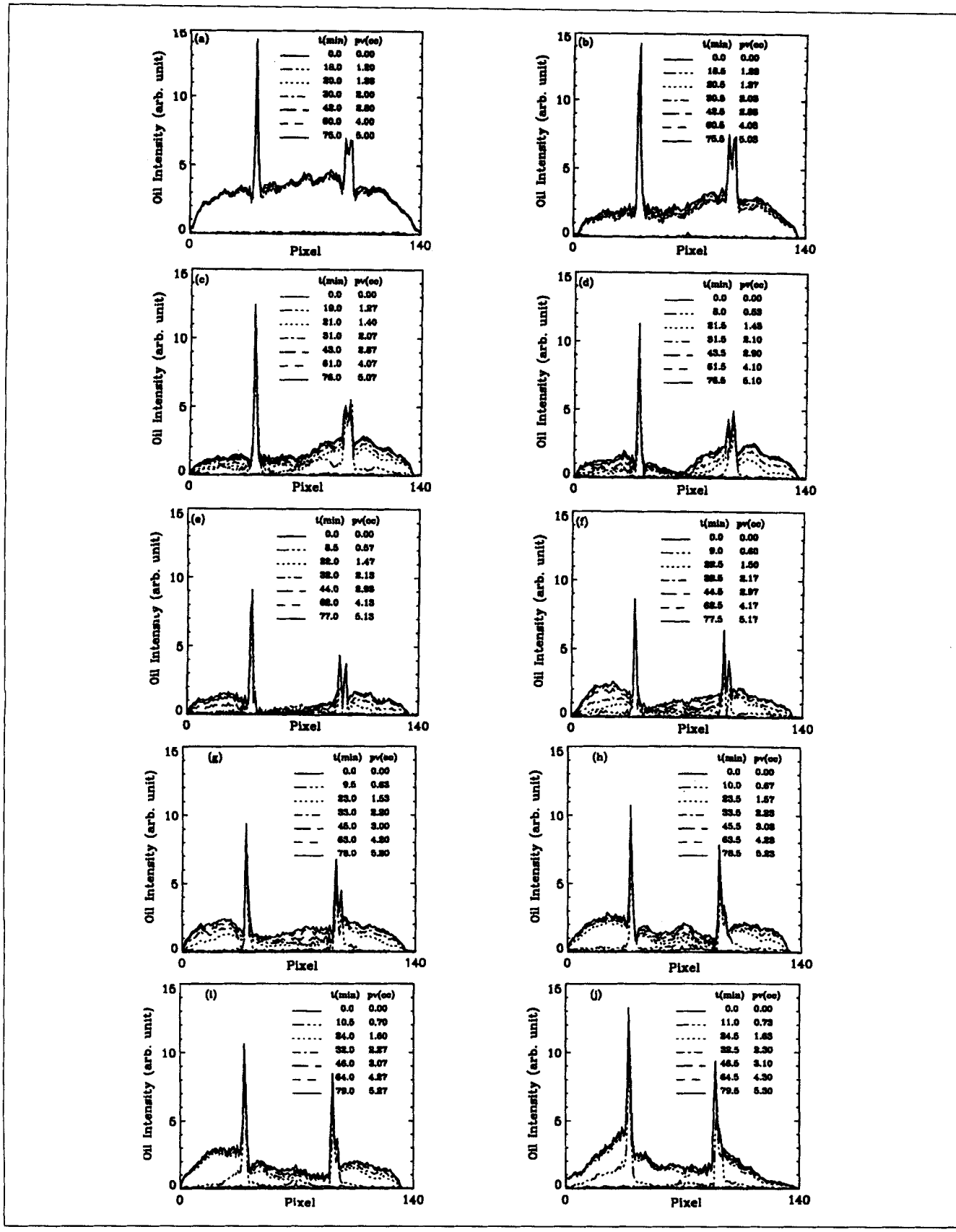

Figure 9. Time-dependent oil intensity profiles of an Arkansas Gold sandstone sample obtained at different times during an experiment with hexadecane displacing D_2O.

The ten plots correspond to 10 locations along the core sample: (a) → (j) corresponds to inlet → outlet.

region near the center of the sample continue to change throughout this experiment, the distributions near the outlet (Figure 9j), as well as near the inlet (Figure 9a), appear to be relatively quickly established. This may be indicative of the more complex situation resulting from the coupling of the flow in the fracture and matrix, as compared to flow in the regions near either end of the sample, which largely takes place within the matrix region. It is also interesting that away from the inlet and outlet, most of the displacement of water by oil has occurred in the extremes of the sample, rather than in the region between the two fractures (Figures 9d–9i).

The two experiments illustrate that fractures can quite profoundly affect multiphase displacement in porous media. The use of noninvasive MRI techniques to monitor displacements in fractured systems could provide important information for developing more complete models and better understanding of these processes.

Conclusions

The noninvasive NMR *TI*-weighted imaging technique is investigated for laboratory characterization of fractures and flow in fractured porous media. This technique can selectively highlight either fracture or porous matrix regions. The effectiveness of the technique has been demonstrated with rock systems having natural or artificial fractures.

Two-phase displacement experiments were conducted to investigate features of multiphase flow in fractured systems. The results showed a much more complicated pattern of displacement than is encountered in a relatively uniform porous medium.

Acknowledgments

This research was supported in part by a University-Industry Cooperative Research Program for Petrophysical and Reservoir Engineering Applications of NMR at Texas A&M University.

Notation

G = imaging gradient strength
k = permeability
M = amplitude of magnetization
M_0 = intrinsic intensity of magnetization
T_1 = longitudinal relaxation time
$T_{1\alpha}$ = T_1 from stretched exponential model
T_2 = transverse relaxation time
TE = echo time
TI_0 = TI that nullifies the signal
$TI_{0\text{fracture}}$ = TI that nullifies the signal in fracture
$TI_{0\text{matrix}}$ = TI that nullifies the signal in matrix

Greek Letters

α = stretch exponent
$\Delta\nu$ = NMR linewidth
ϕ = porosity
θ = orientation angle

Superscripts

exp = experimental value
cal = calculated value

Literature Cited

Banavar, J. R., and L. M. Schwartz, "Probing Porous Media with Nuclear Magnetic Resonance," *Molecular Dynamics in Restricted Geometries*, Chap. 10, J. Klafter and J. M. Drake, eds., p. 273, Wiley, New York (1989).

Brownstein, K. R., and C. E. Tarr, "Spin-Lattice Relaxation in a System Governed by Diffusion," *J. Magn. Reson.*, **26**, 17 (1977).

Bydder, G. M., and I. R. Young, "MR Imaging: Clinical Use of the Inversion Recovery Sequence," *J. Comput. Assist. Tomog.*, **9**(6), 659 (1985).

Callaghan, P. T., *Principles of Nuclear Magnetic Resonance Microscopy*, Clarendon, Oxford (1991).

Chen, S., Liaw, H.-K., and A. T. Watson, "Saturation Dependent Nuclear Magnetic Resonance Spin-Lattice Relaxation in Porous Media and Pore Structure Analysis," *J. Appl. Phys.*, **74**, 1473 (1993a).

Chen, S., Qin, F., Kim, K.-H., and A. T. Watson, "NMR Imaging of Multiphase Flow in Porous Media," *AIChE J.*, **39**(6), 925 (1993).

Chen, S., Qin, F., and A. T. Watson, "Determining Fluid Saturation During Multiphase Flow Experiments by NMR Imaging Techniques," *AIChE J.*, **40**, 1238 (July, 1994).

Dwyer, A. J., J. A. Frank, V. J. Sank, J. W. Reinig, A. M. Hickey, and J. L. Doppman, "Short-TI Inversion-Recovery Pulse Sequence: Analysis and Initial Experience in Cancer Imaging," *Radiology*, **168**, 827 (1988).

Economides, M. J., and K. G. Nolte, *Reservoir Stimulation*, 2nd ed., Prentice-Hall, Englewood Cliffs, NJ (1988).

Fordham, E. J., L. D. Hall, Ramakrishnan, M. R. Sharpe, and C. Hall, "Saturation Gradient in Drainage of Porous Media: NMR Imaging Measurements, *AIChE J.*, **39**(9), 1431 (1994).

Kazemi, H., Gilman, J. R., and Elsharkawy, A. M., "Analytical and Numerical Solution of Oil Recovery From Fractured Reservoirs with Empirical Transfer Functions," *SPERE*, p. 219 (May 1992).

Lu, X., P. Miao, P., A. T. Watson, G. P. Pepin, R. M. Moss, and M. Semmelbeck, M., "X-Ray Computed Tomography Studies of Gas Storage and Transport in Devonian Shale," *AIChE J.*, **40**, 1246 (July, 1994).

Mascalchi, M., G. D. Pozzo, and C. Bartolozzi, "Effectiveness of the Short TI Inversion Recovery (STIR) Sequence in Imaging of Intraedullary Spinal Lesions, *Magn. Reson. Imag.*, **11**, 17 (1993).

Morris, P. G., *Nuclear Magnetic Resonance Imaging in Medicine and Biology*, Clarendon, Oxford (1986).

Watson, A. T., and J. Mudra, "Characterization of Devonian Shales with X-Ray Computed Tomograph," *SPEFE*, p. 209 (Sept. 1994).

Manuscript received Dec. 19, 1994, and revision received Apr. 28, 1995.